VTT Technical Research Centre of Finland

Effect of machining on near surface microstructure and the observation of martensite at the fatigue crack tip in PWR environment of 304L stainless steel

Que, Zaiqing; Huotilainen, Caitlin; Seppänen, Tiia; Lydman, Jari; Ehrnstén, Ulla

Link to publication

Effect of machining on near surface microstructure and the observation of martensite at the fatigue crack tip in PWR environment of 304L stainless steel

Z. Que*, C. Huotilainen, T. Seppänen, J. Lydman, U. Ehrnstén

VTT Technical Research Centre of Finland, Kivimiehentie 3, Espoo 02150, Finland

ABSTRACT

This work highlighted that a ground surface finish and the exposure to a pressurised water reactor (PWR) environment result in a decreased low-cycle fatigue lifetime, an enhanced fatigue crack initiation and an accelerated fatigue crack growth rate of 304 L austenitic stainless steel. A ground surface finish promotes fatigue crack initiation and short crack growth especially in a water environment, due to the highly deformed underlying microstructure with high-angle grain boundaries and the grinding marks on surface. Martensite was observed in the vicinity of secondary crack tips in specimens tested in a simulated PWR primary side environment. The aggregated presence of α'- and ε-martensite in the vicinity of the fatigue crack tip can enhance the material's susceptibility to hydrogen-assisted fatigue cracking. Martensite formation was rarely observed in specimens exposed to high temperature air. The phase transformation from γ-austenite to α'-martensite in the PWR primary environment occurred via the intermediate ε-martensite phase.

1. Introduction

Austenitic stainless steels are extensively utilised in primary circuit pipelines for nuclear power plants (NPP) due to their good general corrosion resistance in high temperature aqueous environments [1,2]. In addition to withstanding prolonged exposure to a pressurised water reactor (PWR) primary side environment (300 °C, 140 bar, 25–35 cc kg^{-1} dissolved hydrogen, 1000 ppm B (as H_3BO_3), 2 ppm Li (as LiOH)), these stainless steels are subjected to non-monotonic cyclic loading conditions, mainly associated with thermal transients, such as the occasional plant shutdown and start-up in NPPs [3]. Laboratory studies indicate that the fatigue life of austenitic stainless steels decreases due to exposure to a light water reactor primary water environment, compared to air or inert environment [4–9]. Like other environmentally assisted degradation mechanisms, environmentally assisted fatigue (EAF) is influenced by a number of environmental (water chemistry, temperature, *etc.*), mechanical (stress state, strain rate, strain amplitude, *etc.*) and material factors (chemical composition, microstructure, *etc.*) [10]. Although extensive studies have been performed, knowledge gaps including the effect of surface finish on fatigue crack initiation, the role of phase transformation in metastable austenitic stainless steels, such as 304 L and the potential for hydrogen-assisted cracking in NPP environments remain [11–15].

Fatigue cracking may be divided into two stages: Stage I initiation and Stage II propagation [1]. The initiation of surface cracks, or microstructurally small cracks (MSCs), often occurs at heterogeneities or localised areas of elevated stress present on the material's surface, e.g. grain, twin or phase boundaries, slip bands, secondary phases, *etc.* [2]. The deformation and microstructural changes of these surface grains can assist fatigue cracking in machined specimens [16]. After the initiation of MSCs, cracks will continue to grow along the primary slip plane at a 45 ° angle to the loading/unloading direction. This is considered to be a part of Stage I fatigue cracking [1]. The growth of MSCs is highly influenced by the local microstructure and, moreover, has been found to be slowed by microstructural features such as grain boundaries (GB), triple points and phase boundaries [17]. In both air and mildly corrosive environments, fatigue striations are usually not visible in Stage I fatigue cracking, but can be observed perpendicular to the direction of crack propagation for Stage II cracking [16,18,19]. As the initiation of fatigue cracks is influenced by mi-

crostructural and surface heterogeneities, surface finish can play a significant role in the portion of the fatigue lifetime spent in the initiation phase [19]. The effect of surface finish on initiation time and fatigue lifetime - particularly the transferability of laboratory testing results on smooth specimens to plant behaviour on components with a machined finish is not fully understood [11]. Moreover, the evaluation of fatigue striations present on the primary fatigue crack fracture surface can provide valuable insight on the fatigue crack growth rate (FCGR) in PWR environments, in addition to providing a direct estimation of the number of cycles to failure [20].

Hydrogen, present in PWR primary water environment (25–50 cc kg^{-1}) and produced as a by-product of corrosion reactions during NPP operation, can be absorbed by the material. In stainless steel, hydrogen, as a proton, is transported across the oxide to the oxide/alloy interface where it can be absorbed by the alloy [21]. After uptake by the alloy, hydrogen is transported within the material via interstitial diffusion, during which hydrogen can interact with the crystal lattice and heterogeneities or defects, including but not limited to grain and phase boundaries, dislocations and stress fields, precipitates, vacancies, *etc.*, present inherently in the material. These sites modify the hydrogen transportation and may result in trapping of hydrogen in the alloy. While the accumulation of hydrogen at these locations can lead to a significant local degradation of mechanical properties of metallic materials [22], the specific role hydrogen plays in low-cycle fatigue (LCF) of austenitic stainless steels in a simulated PWR primary water environment should be investigated further. In addition, when characterizing the morphology of fatigue crack propagation, the presence of fatigue striations is considered to be an indication that the film rupture/slip dissolution mechanism is not the major contributing mechanism for fatigue crack propagation at that location, but can be linked to, for example, hydrogen-enhanced mechanisms affecting the mechanical properties at the crack tip [6,17].

When evaluating the fatigue behaviour and fatigue mechanism of metastable austenitic stainless steels, such as type 304 L, it is important to note that these steels can undergo a deformation-induced phase transformation from austenite (fcc) into α'-martensite (bcc) and ε-martensite (hcp) [12,23]. The presence of deformation induced martensite can render austenitic stainless steels more susceptible to hydrogen-assisted cracking [14,15]. In addition, some authors have reported that hydrogen can enhance the martensitic transformation [3]. The loss of ductility of the stainless steel in a hydrogen-containing environment become more significant with the increasing amount of transformed martensite [3]. The martensite phase transformation process and the mechanism of detrimental effect of hydrogen on the fatigue crack growth (FCG) behaviour in PWR environments require further investigation.

In this work, (i) the effect of a machined surface finish on fatigue crack initiation was investigated through near-surface characterizations and (ii) the phase transformation mechanism and the possible effect of hydrogen was explored by the characterization of secondary fatigue crack tips in specimens tested in a simulated PWR primary environment or a high temperature air (HTA) environment.

2. Material and experimental procedure

2.1. Material, specimen and experiment

This study was carried out within the testing programme framework of the INCEFA-PLUS project. The fatigue behaviour of a solution annealed slab of a nuclear grade austenitic stainless steel type 304 L was investigated in this project [24–27]. The alloys chemical composition can be found in Table 1. The matrix grain size of the investigated material has been measured as ASTM 3–4 and ASTM 3 in the transverse and longitudinal directions, respectively, with approximately 3% of δ-ferrite in volume.

Solid bar specimens for LCF testing were manufactured in the longitudinal direction. Two representative surface finish were investigated – (i) a laboratory polished finish and (ii) ground finish. The polished surface was prepared using the equivalent of 2700 FEPA (Federation of European Producers of Abrasives) standard sandpaper, which resulted in fine axial polishing marks at a 45 ° angle to the loading/unloading direction. The ground finish aimed to simulate the "worst case" scenario roughness of plant components and was produced using an automated grinding bench for cylindrical fatigue test specimens, resulting in circumferential grinding marks along the entire gauge length and transition radius of the fatigue test specimen. Polished specimens are considered to have a nominal average roughness (R_a) and maximum height of the profile (R_t) of 0.04 μm and 0.76 μm, respectively. The measured R_a and R_t of the investigated ground specimens can be found in Table 2. The variability in surface roughness of the ground surface finish is linked to the maximum achievable roughness with regards to a given gauge length diameter. Polished specimens tested in a HTA or simulated PWR primary environment will be referred to as AP and PP, respectively, while ground specimens tested in a HTA or simulated PWR primary environment will be referred to as AG and PG, respectively, from this point forward.

LCF testing was performed in a simulated PWR primary water environment or HTA at 300 °C, see Table 3. Cyclic loading at a strain amplitude (ε_a) of 0.3% or 0.6% ($R = -1$) under nominal total strain control was applied. After inserting specimens into the autoclave or test rig, and achieving the desired environmental conditions, cyclic loading was applied at a strain rate of 1×10^{-4} s^{-1}. The fatigue life (N_f) criteria for failure was defined as the cycle at which the tensile peak stress of a cycle drops by 25% from its steady state tensile peak stress.

2.2. Post-mortem characterisations

After specimen failure, fractographic and microstructural characterisation were performed using complementary microscopy techniques to investigate the EAF cracks developed in stainless steel 304 L in HTA or simulated PWR primary environments. A field emission gun (FEG) scanning electron microscope (SEM) Zeiss Crossbeam 540, equipped with a solid-state four-quadrant backscatter detector and an EDAX Hikari Plus electron backscatter diffraction (EBSD) detector, was used to perform these investigations.

2.2.1. Fatigue striation spacing evaluations

The morphology of the primary fatigue crack was characterised in SEM secondary electron (SE) mode. The main fatigue crack path was first identified on the fracture surface, after which the average striation spacing was measured as a function of crack depth (a). Oxide removal was not performed on the investigated specimens. Factors like environment or strain amplitude can influence the striation/cycle ratio. A general approach with a one cycle: one striation relation in both air and PWR environments was applied for this paper.

2.2.2. Investigation of cross-sections

The role of surface finish on the initiation of fatigue cracks was investigated by cross-section characterisations of the near-surface microstructure of the selected failed specimens, while the role of environment on cracking mechanism was investigated from LCF crack tip observations. Tested specimens were sectioned perpendicular to the primary fatigue crack initiation location in the direction of crack propagation with a mechanical saw, then mounted in

Table 1
Chemical composition (wt.%) of the stainless steel 304 L investigated in this study.

	Fe	C	Mn	Si	S	P	Ni	Cr	Mo	Cu	N
SS 304L	bal.	0.029	1.86	0.37	0.004	0.029	10.0	18.00	0.04	0.02	0.056

Table 2
Fatigue lifetimes and nominal or measured surface roughness (Ra and Rt) of the investigated specimens.

Sample name	N_f(cycles)	$R_a(\mu m)$	$R_t(\mu m)$
AP 0.3%	25,020	0.04[a]	0.76[a]
AG 0.3%	17,768	2.18	25.96
AP 0.6%	5450	0.04[a]	0.76[a]
AG 0.6%	5525	5.20	44.60
PP 0.3%	6547	0.04[a]	0.76[a]
PG 0.3%	4897	1.46	13.65
PP 0.6%	778	0.04[a]	0.76[a]
PG 0.6%	1112	1.74	19.28

[a] indicates nominal value.

Table 3
Nominal high temperature air and simulated PWR environments.

		Air	PWR
T	°C	300 ± 2	300 ± 2
Relative humidity	%	< 30	–
P	bar	atmospheric	150 (min)
[Li] as LiOH	(ppm)	–	(2 ± 0.2) ppm
[B] as B(OH)$_3$	(ppm)	–	1000 ± 100
O_2	(ppb)	–	< 5
H_2	(cc kg^{-1})	–	25–30
pH$_{300 °C}$	-	–	6.95

a conductive resin, before being mechanically ground and polished to a mirror finish with a 0.25 μm diamond paste. The final polishing step was with a 0.04 μm non-crystallizing amorphous colloidal silica suspension.

The near-surface microstructure and secondary fatigue crack tips were investigated using SEM-backscatter electron (BSE) imaging techniques coupled with EBSD. BSE imaging was conducted with the solid-state four-quadrant backscatter detector at an accelerating voltage of 20 keV with a working distance of 4–6 mm. BSE imaging is based on the electron channelling contrast due to the dependence of the BSE signal by the orientation of crystal lattice planes with respect to the incident electron beam [28]. Although the resolution is lower than with transmission electron microscopy, BSE imaging has the advantage of using bulk material and can be used for accessing a larger areas of interest, for example in the vicinity of the crack tip. EBSD mapping was conducted at an accelerating voltage of 15 keV and working distance of 14 mm with a 70 ° tilting angle and a probe current of 1.5 nA. EBSD inversed pole figures (IPF) and kernel average misorientation (KAM) images with scale of 0–5 ° were analysed by the TSL OIM Analysis 8 software.

2.2.3. Evaluation of the effective strain intensity factor

Previous studies have demonstrated that the effective strain intensity factor ($\Delta K_{\varepsilon\text{-}eff}$) presents a good description of FCG, especially in a simulated PWR environment [19,29]. As the $\Delta K_{\varepsilon\text{-}eff}$ is independent of the stress amplitude, it can be defined as

$$\Delta K_{\varepsilon-eff} = f \cdot \Delta \varepsilon_{eff} \cdot \sqrt{\pi a} \tag{1}$$

where $\Delta \varepsilon_{eff}$ is the effective strain range accounting for crack closure and f is the geometrical constant for the stress intensity factor [30,31]. In this study the applied f was defined based on a round

bar specimen with a semi-circular surface crack from Ref. [32],

$$f = \frac{\frac{1.84}{\pi} \cdot \left(\frac{tan[\psi]}{\psi} \right)^{0.5}}{\cos[\psi]} \cdot \left[0.752 + 2.02\varsigma + 0.37 \cdot (1 - \sin[\psi])^3 \right] \tag{2}$$

where $\psi = \frac{\pi a}{4R_0}$ and $\varsigma = \frac{a}{2R_0}$ and R_0 is the starting specimen radius, or in the case of a straight crack front at final fracture, like observed in two of the eight specimens characterised in this study, the f was defined as [32]:

$$f = 0.926 - 1.771\varsigma + 26.421\varsigma^2 - 78.481\varsigma^3 + 87.911\varsigma^4 \tag{3}$$

Bending stress was not considered. The $\Delta \varepsilon_{eff}$ was defined as [30,31]

$$\Delta \varepsilon_{eff} = \Delta \varepsilon + \frac{\sigma_{min}}{E} \tag{4}$$

where $\Delta \varepsilon$ is the nominal strain range, σ_{min} is the minimum stress of the cycle and E is the Young's modulus at 300 °C of the 304 L material used in this study [18]. From this calculation, the crack growth rate, or change in crack depth per cycle (da/dN), for Stage II cracking in a simulated PWR environment can be estimated for the main fatigue crack [20,33]. In addition, the FCGR (da/dN) can be calculated as [30,31]

$$da/dN = D\left(\Delta K_{\varepsilon-eff} \right)^m \tag{5}$$

where the constants D and m are determined by an allometric power-law fitting of the data.

3. Results

3.1. Mechanical behaviour and fatigue lifetime

Strain-controlled LCF tests were performed to assess the EAF behaviour of 304 L stainless steel in HTA and simulated PWR environments. The fatigue crack initiation life as a function of nominal ε_a for the entire testing programme [34], approximately 200 fatigue data points, is presented in Fig. 1. Eight specimens, considered representative of the testing programme, with regards to fatigue behaviour and lifetime for their respective surface and test condition, are highlighted in Fig. 1. These eight specimens are the focus of this paper. The N_f of the investigated specimens is presented in Table 2.

Based upon the analysis of Fig. 1 and Table 2, it can be stated that specimens tested in HTA exhibit longer fatigue lifetimes, compared to those exposed to a simulated PWR primary environment, see Fig. 1. Moreover, the negative impact of high strain amplitude and a ground surface finish, particularly at low ε_a, on fatigue lifetime were found.

3.2. Striation spacing evaluation and effective strain intensity factor

The striation spacing was measured from SEM-SE observations of the main fatigue crack. Fatigue striations very close to the sample surface ($a < 50$ μm) were not observed after testing in a HTA or simulated PWR primary environment. At longer crack depths, fatigue striations were visible for specimens tested in both HTA and simulated PWR environments. Fig. 2 presents the striations observed at a crack depth of 500 μm on polished specimens tested at $\varepsilon_a = 0.6\%$ in (a) HTA (AP 0.6%) and (b) simulated PWR primary
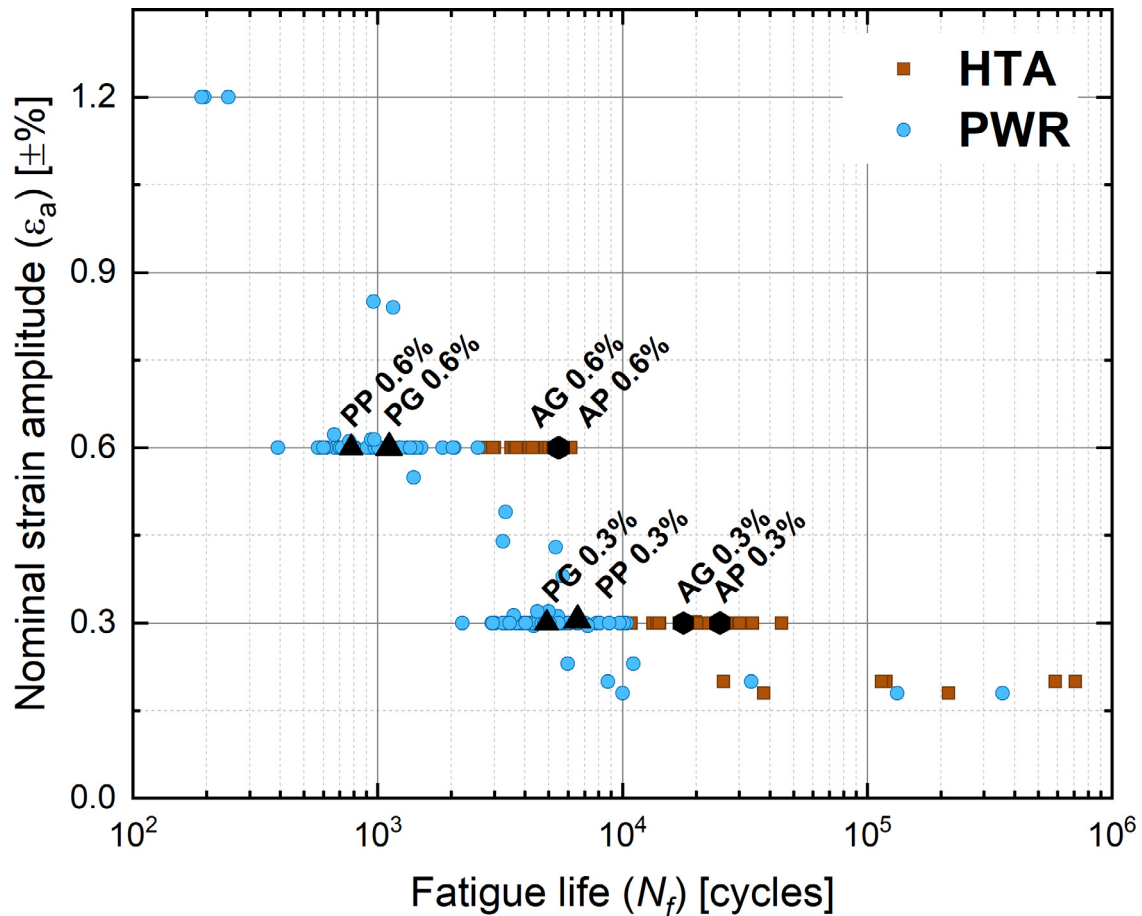
Fig. 1. Fatigue lifetime of specimens tested within the INCEFA-PLUS testing program as a function of nominal εa. The eight representative specimens that have been characterised within this study are indicated in this figure. The points corresponding to the Nf for AG 0.6% and AP 0.6% are overlapping.
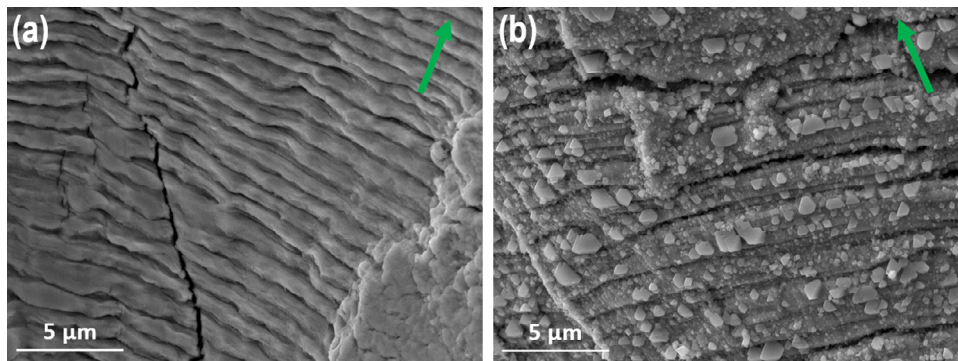

Fig. 2. SEM-SE observations of fatigue striations formed on polished specimens tested in (a) air and (b) PWR environment (AP 0.6% and PP 0.6%) at $a = 500$ μm. The direction of crack propagation is indicated by the green arrow. (For interpretation of the references to color in this figure legend, the reader is referred to the web version of this article.)

environment (PP 0.6%). The fracture surface of PP 0.6% was covered with an oxide scale and oxide crystallites (Fig. 2(b)). The striation spacing as a function of crack depth ($a \leq 3$ mm) for the investigated specimens is presented in Fig. 3(a).

Eqs. (1)–(5) were used to estimate the $\Delta K_{\varepsilon\text{-}eff}$ for the investigated specimens depending on the shape of the crack front. The results are plotted in Fig. 3(b). Only the short crack region ($a \leq 3$ mm) was considered in this analysis, as to remain well within the validity region of the stress intensity factor [32]. The increased strain amplitude and the exposure to PWR environment result in a higher FCGR of 304 L austenitic stainless steel, which is

reflected by the larger striation spacing and da/dN at a given crack depth, see Fig. 3(b).

3.3. Cross-sectional microstructural characterisation

3.3.1. Near-surface observations

Post-mortem microstructural characterisations were performed on polished and ground specimens, after testing in a simulated PWR environment, revealed significant differences in near surface microstructure. Representative SEM-BSE and EBSD micrographs of the cross sections with the polished and ground finish are shown
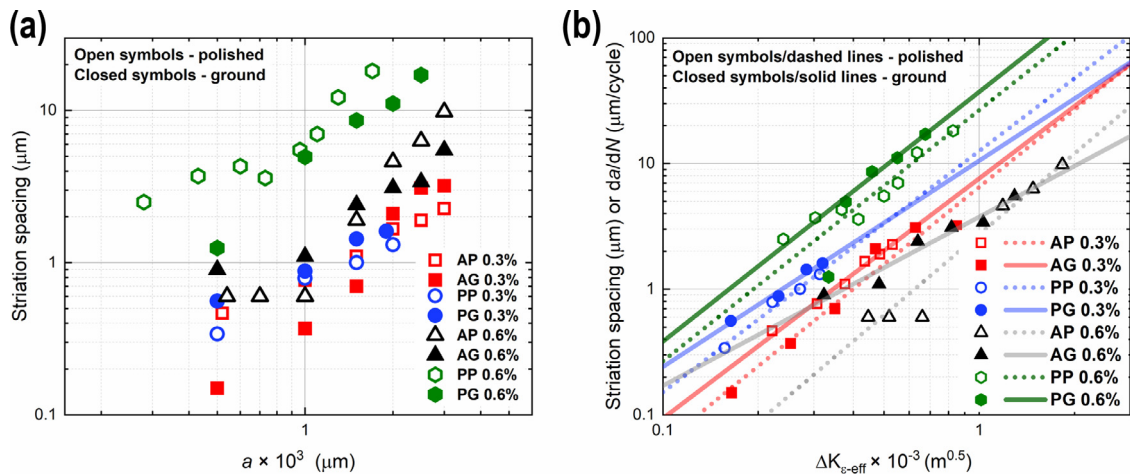
Fig. 3. Striation spacing as a function of (a) crack depth and (b) effective strain intensity factor for short crack depths ($\leq$ 3 mm).

in Fig. 4(a–d) and (e–h), respectively. Secondary fatigue cracks can be seen in these observations.

The presence of a layer of sub-surface deformation, and microstructural gradient, as a result of polishing or grinding operations was observed. The polished surface finish resulted in an ultrafine-grained layer and thin deformation layer extending approximately 1 μm into the specimen (Fig. 4 (c, d)). Nanometric, dense, transgranular cracks, which are parallel to the deformation induced twins, were observed at the sub-surface (Fig. 4(b)). Grinding operations also resulted in an outer ultrafine-grain layer (Fig. 4(e–h)), with a deformation layer extending 10–20 μm into the bulk (Fig. 4(h)), with a set of deformation bands (Fig. 4(f, g)). These deformation bands have a width and spacing of approximately 1 μm and 1.5 μm, respectively. Fig. 4(c, d) and (g, h) highlights the local deformation in the near-surface region. The grinding process resulted in a higher average KAM value than the polished surface finish in the area beyond tens of microns from the sample surface. The grinding process resulted in a much higher surface roughness compared to the polished surface finish.

3.3.2. Crack tip investigations

SEM-BSE micrographs and EBSD maps in Figs. 5 to 7 reveal the deformed microstructures and phases present in the vicinity of secondary fatigue crack tips in specimens tested at $\varepsilon_a = 0.3\%$ in a simulated PWR environment. In Fig. 5(a, b), deformation bands formed parallel to the intersecting GB during cycling. Between the deformation bands, regions of hcp ε-martensite (red) and bcc α'-martensite (blue) can be found. The nucleation of α'-martensite occurs perpendicular to the ε-martensite bands. The morphology of α'-martensite islands can be described as lenticular. As shown in Fig. 5(b, c), ε-martensite bands are forming deformation channels. The α'-martensite islands were enclosed in the deformation band boundaries. Consequently, the cyclic plastic strain is localised in the volumes between the ladder-like α'-martensite islands (Fig. 5(d)). A parallel set of deformation ε-martensite is characterised in Fig. 5(e, f). Moreover, no martensite transformation was observed away from the fatigue crack tip in the matrix.

In Figs. 6(a) and 7(a), two additional representative secondary fatigue cracks, extending over 200 μm into the bulk, can be seen. The bcc α'-martensite (blue) and hcp ε-martensite (red) phases are observed in the vicinity of the crack tip. Deformation band boundaries were characterised by a parallel set of nano-twins (Figs. 6(b, c) and 7(b–g)). The hcp ε-martensite phase is observed inside the deformation band and the α'-martensite nucleation occurs at hcp ε-martensite band intersections (Figs. 6(e, f) and 7(e, f)). In

Figs. 6(h, i) and 7(h, i), the collected and simulated Kikuchi patterns from point A, α'-martensite (Figs. 6(e), 7(e)), and point B, ε-martensite (Figs. 6(e), 7(e)), are presented. In Figs. 6(g) and 7(f), deformation mismatch and strain localisation between the austenite matrix and deformation induced martensite can be seen. In addition, a high density of stacking faults have been observed close to the ε-martensite bands (Fig. 7(g)).

The amount of secondary fatigue cracks on the surface of specimens tested in PWR environment is higher than that tested in HTA. A very limited amount of phase transformation in the vicinity of the fatigue crack tip was observed for specimens tested in HTA at ε_a of 0.3% or 0.6%, i.e. a very small amount of martensite was observed (only in one of the ~40 investigated crack tips, see Fig. 8), unlike frequently observed for specimens tested in a simulated PWR environment (martensite was observed in one third of ~35 investigated crack tips, see Figs. 5–7). The crack tip in the majority of HTA specimens is characterised by mixed planar dislocation structures with poorly-defined wavy boundaries at low strain amplitude ($\varepsilon_a = 0.3\%$) (Fig. 9(a)), while more homogeneous dislocation cell/wall structures are formed at increased strain amplitude ($\varepsilon_a = 0.6\%$) (Fig. 9(b)). The transition from mixed wavy/ planar dislocation structures to dislocation cells occurs as a result of the increasing plastic deformation and cyclic loading [40].

4. Discussion

4.1. Effect of surface finish on fatigue crack initiation

Cross-section observations of the polished and ground specimens revealed clear differences in the near surface microstructures. In a polished specimen, the ultrafine-grained layer formed below the specimen surface (Fig. 4(d)) promotes faster oxidation in a PWR environment, leads to passivation and crack arrest and increases the cracking initiation resistance, which therefore hinders the initiation and short crack growth of EAF cracks [35,36].

Grinding introduces a deformed layer with a steep microstructural gradient in the material. The machining process strongly influences the localisation of plastic deformation and the residual stress state on and under the sample surface, and therefore influences fatigue cracking resistance [37,38]. The ground surface had a much higher surface roughness compared to the polished surface finish (see Table 2), and the grinding marks can become preferential EAF crack initiation sites due to the potential notch effects (Fig. 4(h)), particularly when the location of the surface grinding marks coincide with that of the GBs of the deformed grains. In
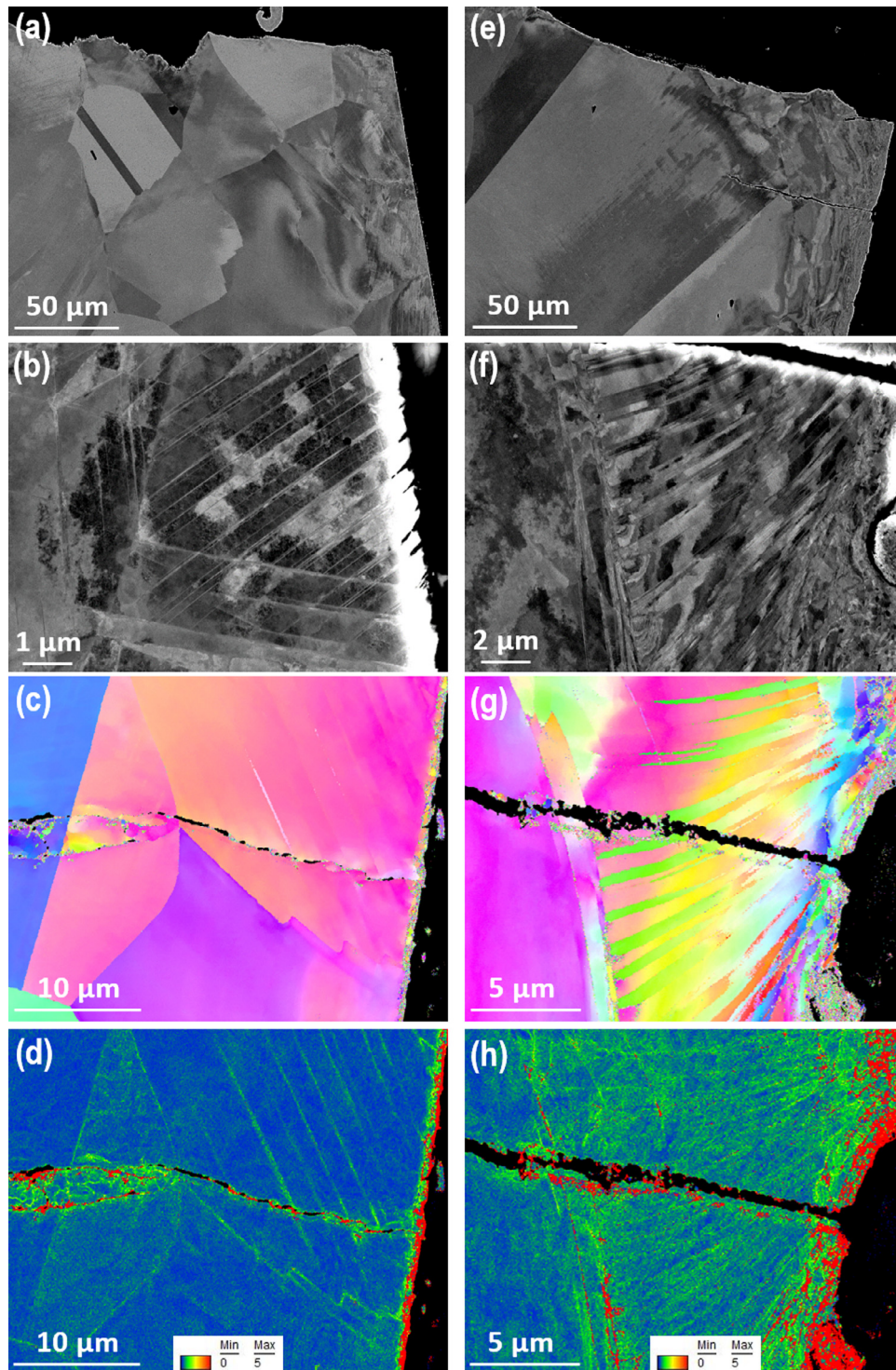
Fig. 4. (a,b,e,f) SEM-BSE and EBSD (c,g) IPF and (d,h) KAM mapping of (a–d) polished and (e–h) ground specimens of 304 L tested at ε_a of 0.3% in a simulated PWR primary water environment. In (b), for a polished sample tested in a PWR environment, a significant amount of nanometric cracks at the slip bands are visible.

this work, the ground surfaces have been found to have higher ratio of high-angle grain boundaries (HAGB) and more extensive slip bands beneath the surface, compared to the polished surface condition (Fig. 4(f, g)). Cracking takes place preferentially in high-energy structural defects, like HAGBs and deformation bands with a high-density of dislocations, while low-angle boundaries, are more resistant [39,40]. Moreover, an elevated stress concentration results in dislocation slip in the ductile bulk metal, which

can accelerate cracking [41]. Dissolution along the slip bands can also promote micro-crack initiation through a crevice corrosion effect [42]. Ultimately these factors would contribute to the enhancement of fatigue crack initiation and decrease in fatigue life of ground specimens. As observed in the experimental testing campaign, specimens with a ground surface finish, in general, have a shorter fatigue lifetime compared to polished specimens with the
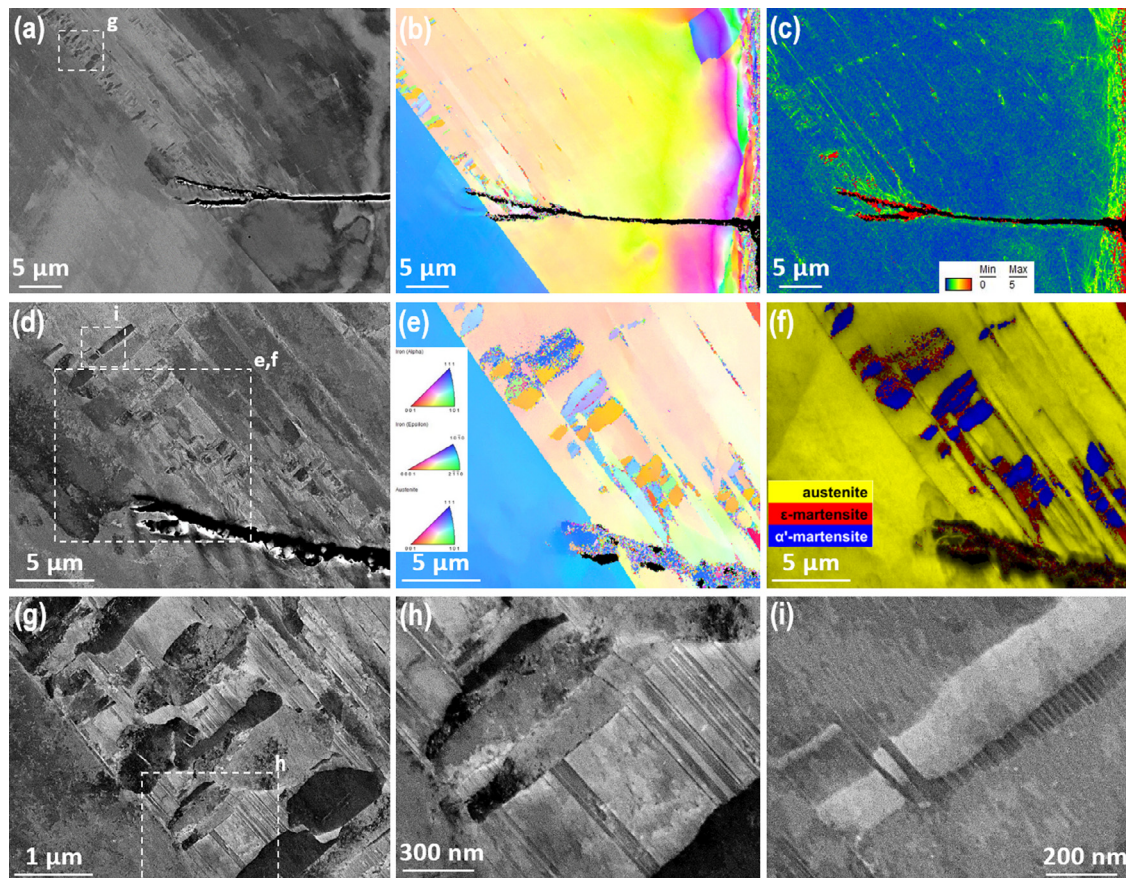
Fig. 5. (a, d, e, f) SEM-BSE and (b, c) EBSD images in the vicinity of a secondary fatigue crack tip from the specimen with ground surfaces of 304 L during LCF testing in a simulated PWR primary water environment (PG 0.3%). EBSD mapping in (e, f) was performed using a step size of 30 nm. The crack tip is ∼ 40 μm from the specimen surface. (For interpretation of the references to color in this figure, the reader is referred to the web version of this article.)

same loading conditions and exposed to the same environment, especially at low ε_a.

4.2. Fatigue crack propagation and growth

After fatigue crack initiation and Stage 1 MSC growth, a transition to Stage II cracking takes place. Stage II fatigue cracking occurs perpendicular to the loading/unloading direction and is characterised by the appearance of fatigue striations [16,18,19]. As the fatigue testing program was carried out as part of a multi-laboratory testing campaign, slightly different sample geometries were used. A method to compensate for geometrical effects when assessing fatigue behaviour was required, therefore $\Delta K_{\varepsilon\text{-eff}}$ was used. One additional feature observed in this study is the absence of Stage I cracking in PWR environment. The classical picture of crack growing along the primary slip plane at a 45 ° angle to the loading/unloading direction is based on observations in air. However, the observations reported for specimens tested in PWR environment in this study do not confirm this. This might indicate that a mechanism that enhances multiple slip in the surface grains, rather than promoting single slip on the most favourably orientated plane, is present in a simulated PWR environment.

In Fig. 3, striation spacing as a function of a and $\Delta K_{\varepsilon\text{-eff}}$ has been presented for polished and ground specimens tested in both HTA and simulated PWR primary environments. While, no significant differences were observed in striation spacing with regards to surface finish, both environment and strain amplitude appear to play a role. At shorter crack depths, specimens tested in a simulated PWR primary environment and/or at higher strain amplitudes ($\varepsilon_a = 0.6\%$) present larger striation spacing than their air tested or

$\varepsilon_a = 0.3\%$ counter parts at similar crack depths. The observation that surface finish had no impact on striation spacing, e.g. fatigue crack propagation, is in agreement with the consensus that surface finish mainly affects crack initiation and MSC formation.

The PWR environment can influence both the MSCs initiation (up to about 250 μm) and mechanically small crack growth (beyond 250 μm). For an estimation of the effect of PWR environment on these two stages, the pair PP 0.3% (Nf = 6547 cycles and da/dN = 3.1 μm/cycle when $\Delta K_{\varepsilon-eff}$ is 0.5 × 10^{-3} m$^{0.5}$) and AP 0.3% (Nf = 25,020 cycles and da/dN = 1.6 μm/cycle when $\Delta K_{\varepsilon-eff}$ is 0.5 × 10^{-3} m$^{0.5}$) was taken as an example. The mechanically small crack growth rate is only about a factor of 2 greater in PWR than in air. Thus, the environmental effect on MSCs needs to be >>2 as the experimental F$_{en}$ for engineering crack initiation (approximately 3 mm) is roughly 4.

4.3. Martensite formation and possible effect of hydrogen on fatigue crack propagation

In this work, the number of secondary fatigue cracks on the surface of specimens tested in a simulated PWR primary environment is higher than that of specimens tested in HTA. Exposure to a simulated PWR primary water environment systematically results in a reduction of fatigue life and cracking resistance. The fatigue life reduction by the exposure to a simulated PWR is in part caused by the formation of martensite phases in the vicinity of the fatigue crack tip, and thus the possible effect of hydrogen should be discussed. Here, the main hydrogen term source is considered to be
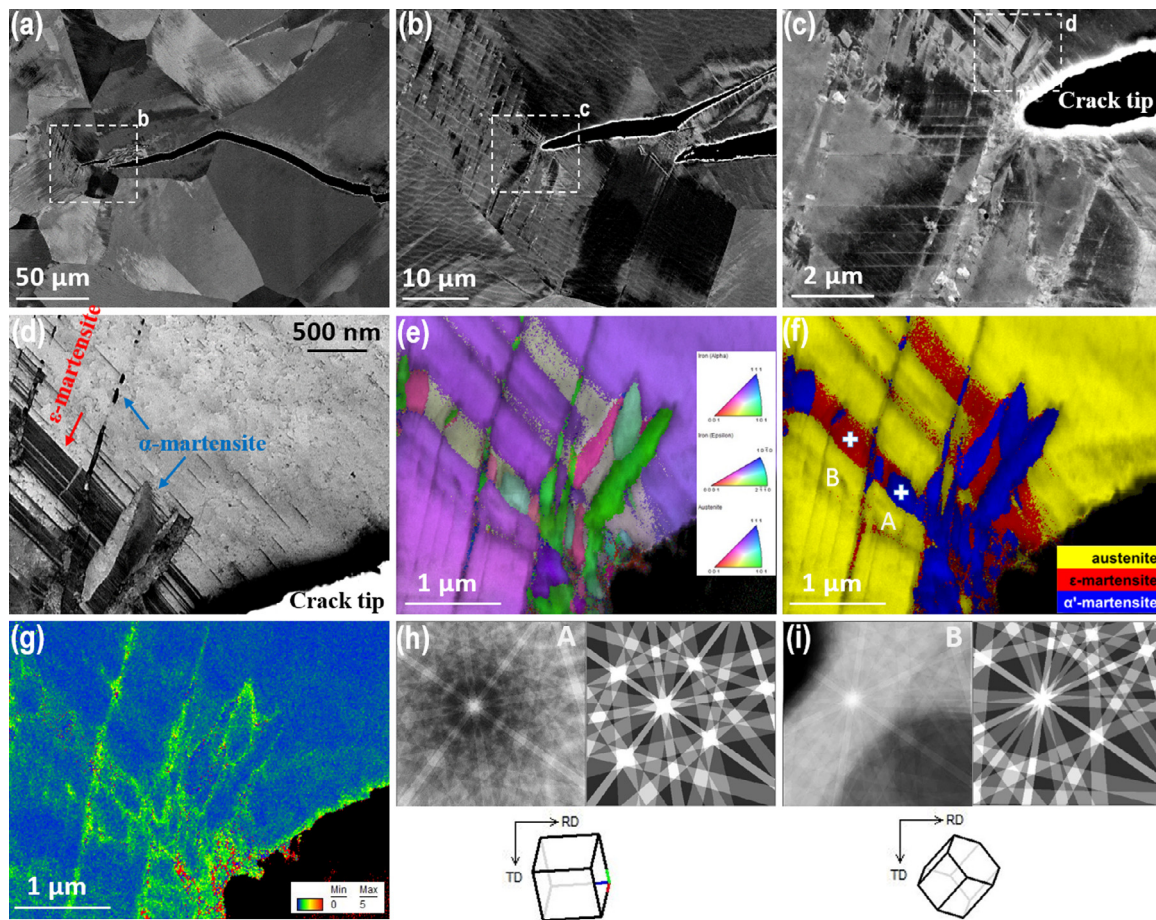
Fig. 6. (a–d) SEM-BSE and (e–g) EBSD images of the fatigue crack tip from the specimen of 304 L during LCF testing in a simulated PWR primary water environment (PG 0.3%). (h, i) are the collected and simulated kikuchi patterns from points A and B in (f), respectively. EBSD mapping was performed using a step size of 20 nm. The crack tip is ∼ 320 μm from the specimen surface. (For interpretation of the references to color in this figure, the reader is referred to the web version of this article.)

the corrosion reactions taking place in a simulated PWR primary environment.

Aggregated phase transformation, i.e. austenite to martensite, was observed in the vicinity of the crack tip for specimens tested in a simulated PWR environment. Indications of phase transformation in HTA tested specimens was rarely observed, regardless of strain amplitude. The presence of hydrogen in the simulated PWR environment can (i) reduce the stacking fault energy [43,44], (ii) increase the density and fraction of ε-martensite subject to an identical strain, compared to in a hydrogen-free condition [43], and (iii) promote the deformation induced $\gamma \rightarrow \varepsilon$ martensitic transformation. The deformation induced phase transformation, from fcc austenite to bcc α'-martensite, can occur either directly ($\gamma \rightarrow \alpha'$) or through the formation of hcp ε martensite ($\gamma \rightarrow \varepsilon \rightarrow \alpha'$) [45,46]. Bogers reported that the transformation of $\gamma \rightarrow \alpha'$ takes place directly when two shear strain components act simultaneously in the fcc lattice [47], although this may not be the case in this study. Observations in this work, instead, revealed that the formation of α'-martensite is related to the prior nucleated ε-martensite, which acts as the intermediate phase [48]. An evident formation of needle-like ε-martensite can take place at the initial state of deformation and preferentially nucleates at the boundaries between the austenite matrix and deformation bands, deformation twins, and/or nearby GBs [49,50,51]. ε-martensite forms via the re-arrangement of stacking faults on every second {111} plane [52]. The needle-like ε-martensite are mostly formed locally in the active slip systems and tilted at a degree of 45 ° to the loading/unloading direction due to the prevailing maximum Schmid

factor [23,53,54], as found in this work. At the intersection point of needle-like ε-martensite, α'-martensite nucleates [55,56].

The fatigue cracking is enhanced by the deformation inconsistence between austenite and α'-martensite during cyclic loading, due to the much higher hardness of α'-martensite than austenite. In addition to being at the root of martensite transformation at the crack tip, the possible accumulation of hydrogen at the transformed martensite/austenite interfaces may lead to an increased FCGR in the material [3]. FCGR was not specifically investigated in this study and thus will not be discussed further. A lower EAF resistance of austenitic stainless steels in hydrogen containing high temperature water than in high dissolved oxygen hot water was reported in Ref. [17]. Nygren also reported an accelerated fatigue failure in 304 steel with hydrogen gas charging [44]. In the presence of hydrogen, fatigue cracks can grow continuously during loading before the cracking opening displacement can reach its maximum value. Therefore, at the maximum load, a sharper crack tip in the presence of hydrogen can be expected than in its absence [57]. Local strain-induced martensitic transformation in the vicinity of crack tips provides a potential hydrogen diffusion passage [58]. Due to the high solubility and low hydrogen diffusivity in austenite matrix and the comparatively low hydrogen solubility and high diffusivity in α'-martensite, the hydrogen can accumulate at the phase boundary or interface between the austenite and α'-martensite [59,60]. Consequently, the crack may continue to propagate along the α'-martensite/austenite interface, resulting from the weak interatomic bonding subject to exterior stress in the presence of hydrogen [61] and the activation of hydrogen induced slip defor-
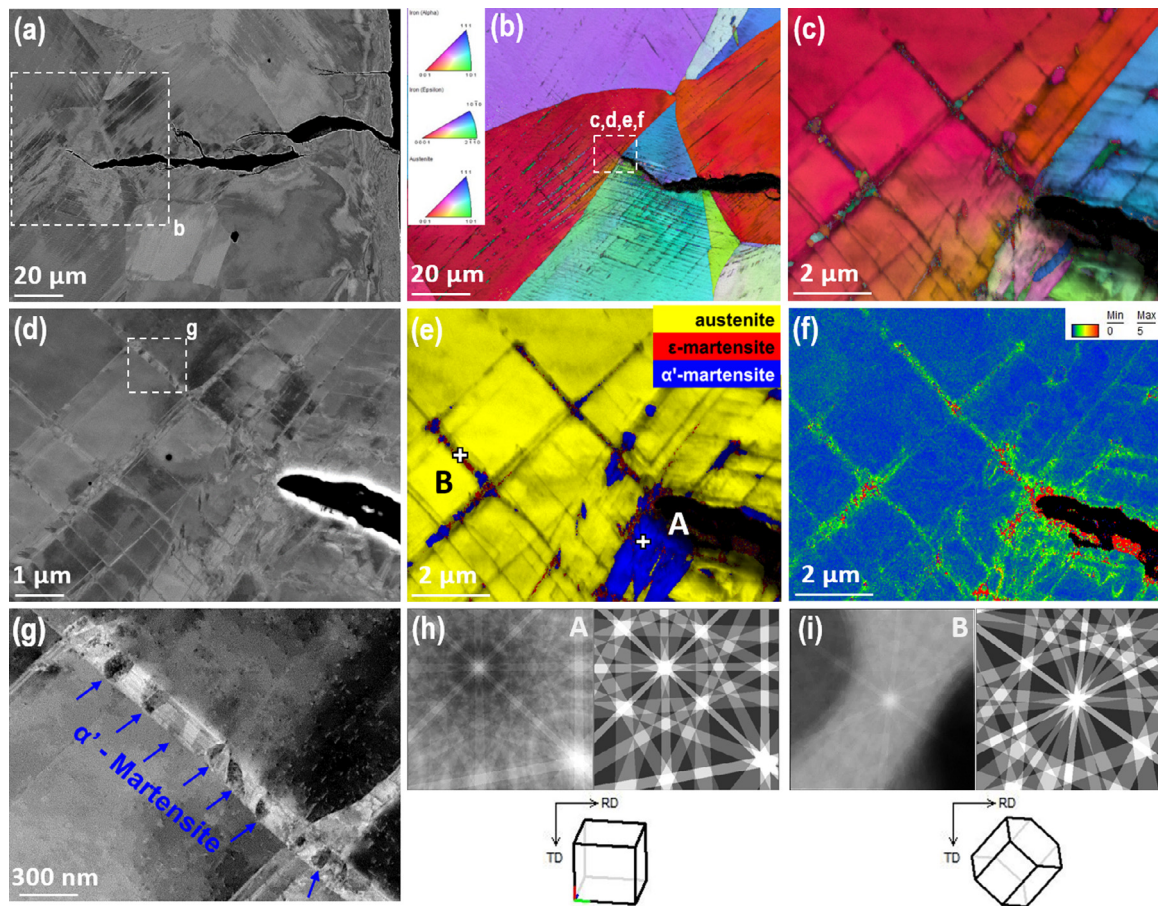
Fig. 7. (a,d,g,h,i) SEM-BSE and EBSD (b,c) IPF, (e) phase and (f) KAM images in the vicinity of a secondary fatigue crack tip formed in 304 L during LCF testing in a simulated PWR primary water environment (PG 0.3%). The collected and simulated Kikuchi patterns from point A and B in (e) are presented in (j) and (k), respectively. EBSD mapping was performed using a step size of 20 nm. The crack tip is ∼ 200 μm from the specimen surface. (For interpretation of the references to color in this figure, the reader is referred to the web version of this article.)
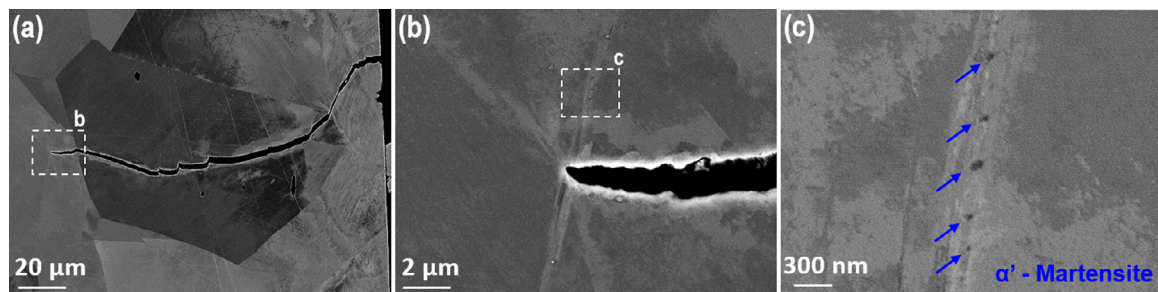

Fig. 8. (a-c) SEM-BSE in the vicinity of a secondary fatigue crack tip formed in 304 L during LCF testing in HTA (AP 0.3%). A very limited amount (1 in ∼40 investigated crack tips) of phase transformation in the vicinity of the fatigue crack tip was observed for specimens tested in HTA. Additionally, the scope of the martensite formation in HTA was very local. The crack tip is ∼ 150 μm from the specimen surface.

mation [62]. α'-martensite promotes hydrogen-assisted crack initiation and propagation along the slip bands and twin boundaries and enhances the FCGR during cycling loading [63]. Moreover, the presence of fatigue striations is considered to be an indication that hydrogen-enhanced mechanisms affecting fatigue cracking [6,17]. A schematic diagram of hydrogen-martensite interactions on EAF susceptibility and cracking behaviour of austenitic stainless steel 304 L is presented in Fig. 10. It should be noted that though both ε-martensite and α'-martensite are formed during the deformation in 304 L, ε-martensite is considered to have little effects on the hydrogen embrittlement [64].

Kamaya [65] investigated the role of martensite transformation on the fatigue life of a 20% cold worked (resulting in martensite

transformation in the bulk material) austenitic stainless steel type 316 in PWR environment but an effect of martensite on the fatigue life was not revealed. However, this is likely linked to a very different material stability and martensite formation process in stainless steel 316 versus 304 L and moreover, localisation of martensite in the bulk versus at the crack tip, and thus different interaction of martensite and hydrogen in the respective system. As discussed above, extensive studies [43,44,48,57,63] have shown the role of martensite formation on the reduction of fatigue lifetime of 304 stainless steel but the majority of these tests were done in hydrogen charged condition at relatively low temperatures. To the knowledge of the authors, this paper is one of few works to directly reveal the formation process of α'- and ε-martensite in the
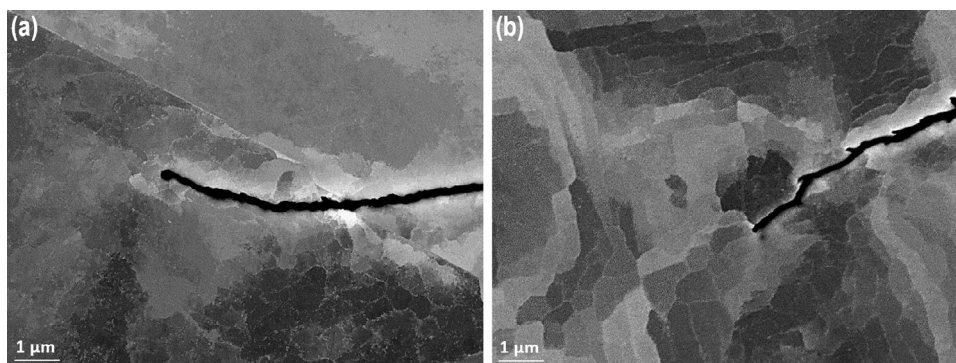
Fig. 9. SEM-BSE images of dislocation structures developed at the crack tip in stainless steel 304 L during LCF testing in HTA at ε_a of (a) 0.3% and (b) 0.6%. The crack tips are ~130 µm and ~110 µm from the specimens' surface for AG 0.3% and AG 0.6%, respectively.
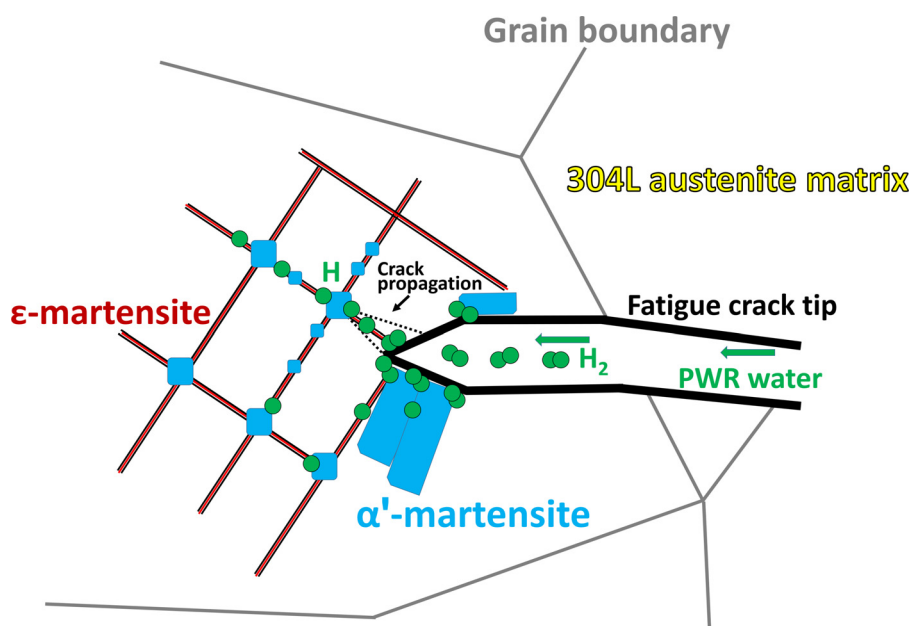

Fig. 10. Martensite formation and its interaction with hydrogen in the vicinity of the fatigue crack tip. α'-martensite initiates at the intersections of ε-martensite. After the dissociation of molecular hydrogen due to the corrosion reaction, atomic hydrogen will be absorbed by and diffuse in the material, where it will accumulate at the phase interfaces, e.g. martensite/austenite boundaries, and other microstructural heterogeneities. The LCF crack can continue to propagate along the martensite/austenite interface.

vicinity of the LCF crack tip and its potential influence on the fatigue life of 304 L steel at high temperature in a simulated PWR primary water environment.

It is worth noting that although ground surface finish, an increased strain amplitude and the exposure to a simulated PWR primary side environment all result in a decreased LCF lifetime, the ground surface finish or an increased strain amplitude did not seem to play a role in the formation of martensite in the vicinity of the LCF crack tip. The effect of surface finish is only evident on the fatigue crack initiation whereas that of martensite formation and possible effect of hydrogen is more significant on the fatigue crack propagation, regardless of strain amplitude or surface finish.

5. Conclusions and perspectives

The effects of surface finish and environment on the LCF behaviour in a nuclear grade 304 L austenitic stainless steel were evaluated by the cross-sectional near-surface and fatigue crack tip characterisations of the round bar specimens tested at 300 °C in simulated PWR primary water and HTA environments. The main conclusions can be summarised as follows:

- Ground surface finish, high strain amplitude and the PWR environment lead to a decrease in fatigue lifetime, specifically with the ground surface finish and simulated PWR environment enhancing fatigue crack initiation and the simulated PWR environment and increased strain amplitude resulting in an increased FCGR.
- Phase transformation was observed in the vicinity of the fatigue crack tip of specimens tested in a simulated PWR primary environment.
  ○ Phase transformation, from γ-austenite to α'-martensite occurred via the intermediate ε-martensite phase.
  ○ Phase formation was rarely observed in specimens tested in HTA.
- The enhanced fatigue crack propagation rate in the hydrogen-containing simulated PWR primary environment is potentially due to the aggregated presence of α'- and ε-martensite in the vicinity of the crack tip and their susceptibility to hydrogen-assisted fatigue cracking.

Future studies could include target experimental testing (e.g. hydrogen pre-charged specimens in air, non-charged specimen in various high-temperature aqueous environments with different levels of dissolved hydrogen and testing of additional stainless

steels that have different stabilities, such as stainless steel type 316 L. Moreover, investigations into martensite formation via X-ray diffraction method and the identification of trapped hydrogen in the vicinity of the crack tip would provide insight to the LCF behaviour of austenitic stainless steels in a simulated PWR primary environment.

Data availability

The data that support the findings of this study are available from the corresponding author upon reasonable request.

Declaration of Competing Interest

The authors declare that they have no known competing financial interests or personal relationships that could have appeared to influence the work reported in this paper.

CRediT authorship contribution statement

Z. Que: Conceptualization, Visualization, Funding acquisition, Formal analysis, Data curation, Writing – original draft, Writing – review & editing. **C. Huotilainen:** Conceptualization, Visualization, Funding acquisition, Formal analysis, Data curation, Writing – original draft, Writing – review & editing. **T. Seppänen:** Conceptualization, Visualization, Formal analysis, Data curation, Writing – review & editing. **J. Lydman:** Funding acquisition, Formal analysis, Data curation. **U. Ehrnstén:** Formal analysis, Data curation.

Acknowledgments

References

[1] P. Forsyth, A two-stage process of fatigue-crack growth, in: Proceedings of the Crack Propagation Symposium, 1, Cranfield, 1962, pp. 76–94.

[2] N. Frost, K. Marsh and L. Pook, Metal Fatigue, Clarendon Press, 1974.

[3] W. Karlsen, "The role of non-monotonic loading in EAC - a literature review," VTT Report, VTT-R-00867-12, Espoo, Finland, 2012.

[4] R. Alain, P. Violan, J. Mendez, Low cycle fatigue behaviour in vacuum of a 316L type austenitic stainless steel between 20 and 600°C part I: fatigue resistance and cyclic behaviour, Mater. Sci. Eng. A 229 (1–2) (1997).

[5] Japan Society of Mechanical Engineers, Tokyo (Japan), "Codes for nuclear power generation facilities - environmental fatigue evaluation method for nuclear power plants (S NFI-2009)," ISBN 4-88898-144-2, 2006.

[6] O. Chopra and G. Stevens, "Effect of LWR water environments on the fatigue life of reactor materials," (NUREG/CR-6909, Revision 1) – Final Report, 2018.

[7] H. Kanasaki, R. Umehara, H. Mizuta, T. Suyama, Fatigue lifes of stainless steels in PWR primary water, in: Proceedings of the 14th International Conference on Structural Mechanics in Reactor Technology (SMiRT 14), Lyon, France, 1997.

[8] J. Solin, J. Alhainen, E. Karabaki, W. Mayinger, Effects of hot water and holds on fatigue of stainless steel, in: Proceedings of the ASME Pressure Vessels and Piping Conference (PVP2016), Vancouver, British Columbia, Canada, 2016.

[9] T. Seppänen, J. Alhainen, E. Arilahti, J. Solin, Low cycle fatigue (EAF) of AISI 304L and 347 in PWR water, in: Proceedings of the ASME Pressure Vessels and Piping Conference (PVP2018), Prague, Czech Republic, 2018.

[10] P. Spätig, M. Heczko, T. Kruml, H. Seifert, Influence of mean stress and light water reactor environment on fatigue life and dislocation microstructures of 316L austenitic steel, J. Nucl. Mater. 509 (2018) 15–28.

[11] Electric Power Research Institute, "Environmentally assisted fatigue (EAF) knowledge gap analysis: update and revision of the EAF knowledge gaps," Technical Report 1026724, 2018 Palo Alto, CA, USA.

[12] G. Fonseca, S. Oliveira, J. Chaves, P. Leite, F. Silva, L. Lopes, Study of martensitic transformation in 304L austenitic stainless steel after tensile and low cycle fatigue tests, J. Mater. Sci. Res. 9 (1) (2020) 22–31.

[13] H. Cho, B. Kim, I. Kim, C. Jang, D. Jung, Fatigue life and crack growth mechanisms of the type 316LN austenitic stainless steel in 310°C deoxygenated water, J. Nucl. Sci. Technol. 44 (7) (2007) 1007–1014.

[14] L. Tsay, S. Yu, R. Huang, Effect of austenite instability on the hydrogen-enhanced crack growth of austenitic stainless steels, Corros. Sci. 49 (2007) 2973–2984.

[15] G. Han, J. He, S. Fukuyama, K. Yokogawa, Effect of strain-induced martensite on hydrogen environment embrittlement of sensitized austenitic stainless steels at low temperatures, Acta Mater. 46 (13) (1998) 4559–4570.

[16] P.H. DeVries, K.T. Ruth, D.P. Dennies, Counting on fatigue: striations and their measure, J. Fail. Anal. Prev. 10 (2) (2010) 120–137.

[17] O. Chopra, Mechanism and Estimation of Fatigue Crack Initiation in Austenitic Stainless Steels in LWR Environments, Nuclear Regulatory Commission, Washington DC, USA, 2002 NUREG/CR-6787 (ANL-01/25) for U.S.

[18] J.R. Davis, Metals Handbook, Desk Edition, 2nd Ed., ASM International, 1998.

[19] O. Chopra and W. Shack, "Review of the margins for ASME code fatigue design curves – effects of surface roughness and material variability," NUREG/CR-6815, ANL-02/39, Argonne, IL, USA, 2003.

[20] T. Poulain, Fatigue Oligocyclique D'un Acier Inoxydable Austenitique 304L : Influence De L'etat De Surface Et De Signaux De Chargement En Milieu Eau Primaire REP, ISAE-ENSMA Ecole Nationale Supérieure de Mécanique et d'Aérotechique, 2005.

[21] M. Dumerval, S. Perrin, L. Marchetti, M. Tabarant, F. Jomard, Y. Wouters, Hydrogen absorption associated with the corrosion mechanism of 316L stainless steels in primary medium of pressurized water reactor (PWR), Corros. Sci. 85 (2014) 251–257.

[22] Z. Que, H. Seifert, P. Spätig, A. Zhang, J. Holzer, G. Rao, S. Ritter, Effect of dynamic strain ageing on environmental degradation of fracture resistance of low-alloy RPV steels in high-temperature water environments, Corros. Sci. 152 (2019) 172–189.

[23] C. Müller-Bollenhagen, M. Zimmermann, H.J. Christ, Very high cycle fatigue behaviour of austenitic stainless steel and the effect of strain-induced martensite, Int. J. Fatigue 32 (2010) 936–942.

[24] M. Bruchhausen, G. Dundulis, A. McLennan, S. Arrieta, T. Austin, R. Cicero, W.J. Chitty, L. Doremus, M. Ernestova, A. Grybenas, C. Huotilainen, J. Mann, K. Mottershead, R. Novotny, F.J. Perosanz, N. Platts, J.C. le Roux, P. Spätig, C. Celeizábal, Characterisation of austenitic stainless steels with regard to environmentally assisted fatigue in simulated light water reactor conditions, Metals (Basel) 11 (2) (2021) 307.

[25] M. Bruchhausen, A. McLennan, R. Cicero, C. Huotilainen, K. Mottershead, J.C. le Roux, M. Vankeerberghen, Environmentally assisted fatigue data from the INCEFA-PLUS project, in: Proceedings of the ASME Pressure Vessels & Piping Conference (PVP2019), San Antonio, Texas, USA, 2019.

[26] M. Bruchhausen, A. McLennan, R. Cicero, C. Huotilainen, K. Mottershead, J.C. le Roux, M. Vankeerberghen, INCEFA-PLUS project: review of the test programme, in: Proceedings of the ASME Pressure Vessels & Piping Conference (PVP2020), Minneapolis, Minnesota, USA, 2020.

[27] K. Mottershead, M. Bruchhausen, S. Cicero, S. Cuvilliez, INCEFA-PLUS: increasing safety in NPPs by covering gaps in environmental fatigue assessment (PVP2020-21220), in: Proceedings of the ASME Pressure Vessels & Piping Conference, 2020 Virtual.

[28] S. Zaefferer, N. Elhami, Theory and application of electron channelling contrast imaging under controlled diffraction conditions, Acta Mater. 75 (2014) 20–50.

[29] S.R. Haigh, A strain intensity approach to high temperature fatigue crack growth and failure, Mater. Sci. Eng. 36 (1) (1978) 133–137.

[30] M. Kamaya, M. Kawakubo, Strain-based modelling of fatigue crack growth – an experimental approach for stainless steel, Int. J. Fatigue 44 (2012) 131–140.

[31] M. Kamaya, Low-cycle fatigue crack growth prediction by strain intensity factor, Int. J. Fatigue 72 (2015) 80–89.

[32] AmericanPetroleum Institute, "Recommended Practice for Fitness-for-Service (API 579)," American Petroleum Institute, 2000.

[33] L. de Baglion de la Dufferie, Comportement Et Endommagement En Fatigue Oligocyclique D'un Acier Inoxydable Austénitique 304L en Fonction De L'environnement (vide, air, Eau Primaire REP), ISAE-ENSMA École Nationale Supérieure de Méchanique et d'Aérotechnique, 2011.

[34] INCEFA-PLUS, "Low Cycle Fatigue - Strain Control Test Data for AISI 304L ar Material At 300°C," MatDB, European Commission JRC, 2019.

[35] H. Seifert, S. Ritter, H. Leber, Corrosion fatigue crack growth behaviour of austenitic stainless steels under light water reactor conditions, Corros. Sci. 55 (2011) 61–75.

[36] Z. Mei, J. Morris, Analysis of transformation-induced crack closure, Eng. Fract. Mech. 39 (1991) 569–573.

[37] S. Ziemniak, M. Hanson, P. Sander, Electropolishing effects on corrosion behaviour of 304 stainless steel in high temperature, hydrogenated water, Corros. Sci. 50 (2008) 2465–2477.

[38] Z. Que, L. Volpe, A. Toivonen, G. Burke, F. Scenini, U. Ehrnstén, Effects of surface treatments on environmentally-assisted cracking susceptibility of alloy 182 in BWR environment, Corros. Sci. 188 (2021) 109555.

[39] W. Karlsen, G. Diego, B. Devrient, Localised deformation as a key precursor to initiation of intergranular stress corrosion cracking of austenitic stainless steels employed in nuclear power plants, J. Nucl. Mater. 406 (2010) 138–151.

[40] P. Lin, G. Palumbo, U. Erb, Influence of grain-boundary-character-distribution on sensitisation and intergranular corrosion of Alloy-600, Scr. Metall. Mater. 33 (9) (1995) 1387–1392.

[41] W. Karlsen, "Deformation microstructures of fatigued and annealed Ti-stabilized austenitic stainless steel," VTT Report, VTT-R-09487-10, Espoo, Finland, 2011.

[42] S. Xu, X. Wu, E. Han, W. Ke, Y. Katada, Crack initiation mechanisms for low cycle fatigue of type 316Ti stainless steel in high temperature water, Mater. Sci. Eng. A 490 (1–2) (2008) 16–25.

[43] M. Koyama, N. Terao, K. Tsuzaki, Revisiting the effects of hydrogen on deformation-induced γ-ε martensitic transformation, Mater. Lett. 249 (2019) 197–200.

[44] K. Nygren, A. Nagao, P. Sofronis, I. Robertson, The role of microstructure in hydrogen-induced fatigue failure of 304 austenitic stainless steel, Metall. Mater. Trans. A (2020) 51A.

[45] V. Mazánová, M. Heczko, V. Škorík, A. Chlupová, J. Polák, T. Kruml, Microstructure and martensitic transformation in 316L austenitic steel during multiaxial low cycle fatigue at room temperature, Mater. Sci. Eng. A 767 (2019) 138407.

[46] Y. Ju, M. Koyama, T. Sawaguchi, K. Tsuzaki, H. Noguchi, Effects of e-martensitic transformation on crack tip deformation, plastic damage accumulation, and slip plane cracking associated with low-cycle fatigue crack growth, Int. J. Fatigue 103 (2017) 533–545.

[47] A. Bogers, W. Burgers, Partial dislocations on (110) planes in bcc lattice + transition of fcc into bcc lattice, Acta Metall. 12 (2) (1964) 255–261.

[48] K. Tsuzaki, E. Nakanishi, T. Maki, I. Tamura, Low-cycle fatigue behaviour in metastable austenitic steel accompanying deformation-induced martensitic transformation, Trans. ISIJ 23 (1983) 834–841.

[49] A. Glage, A. Weidner, H. Biermann, Effect of austenite stability on the low cycle fatigue behaviour and microstructure of high alloyed metastable austenitic cast TRIP steels, Procedia Eng. 2 (2010) 2085–2094.

[50] Y. Shen, X. Li, X. Sun, Y. Wang, L. Zuo, Twinning and martensite in a 304 austenitic stainless steel, Mater. Sci. Eng. A 552 (2012) 514–522.

[51] N. Nakada, H. Ito, Y. Matsuoka, T. Tsuchiyama, S. Takaki, Deformation-induced martensitic transformation behaviour in cold-rolled and cold-drawn type 316 stainless steels, Acta Mater. 58 (3) (2010) 895–903.

[52] X. Yang, S. Sun, T. Zhang, The mechanism of bcc alpha ′ nucleation in single hcp epsilon laths in the fcc gamma ->hcp epsilon ->bcc alpha ′ martensite phase transformation, Acta Mater. 95 (2015) 264–273.

[53] Y. Ju, M. Koyama, T. Sawaguchi, K. Tsuzuki, H. Noguchi, *In situ* microscopic observations of low-cycle fatigue-crack propagation in high-Mn austenitic alloys with deformation-induced ε-martensitic transformation, Acta Mater. 112 (2016) 326–336.

[54] Z. Ma, J. Liu, G. Wang, H. Wang, Y. Wei, H. Gao, Strength gradient enhances fatigue resistance of steels, Sci. Rep. 6 (2016).

[55] C. Blochwitz, S. Jacob, W. Tirschler, Grain orientation effects on the growth of short fatigue cracks in austenitic stainless steel, Mater. Sci. Eng. A 496 (1–2) (2008) 59–66.

[56] U. Krupp, I. Roth, H.J. Christ, M. Kuebbeler, C. Fritzen, *In situ* SEM observation and analysis of martensitic transformation during short fatigue crack propagation in metastable austenitic steel, Adv. Eng. Mater. 12 (4) (2010) 255–261.

[57] T. Kanezaki, C. Narazaki, Y. Mine, S. Matsuoka, Y. Murakami, Effects of hydrogen on fatigue crack growth behaviour of austenitic stainless steels, Int. J. Hydrogen Energy 33 (2008) 2604–2619.

[58] H. Zhang, Y. Li, W. Liang, L. Zheng, Observation of hydrogen diffusion channel and hydrogen trap in 304 austenitic stainless steel, Mater. Lett. 290 (129453) (2021).

[59] L. Queiroga, G. Marcolino, M. Santos, G. Rodrigues, C. Santos, P. Brito, Influence of machining parameters on surface roughness and susceptibility to hydrogen embrittlement of austenitic stainless steels, Int. J. Hydrogen Energy 44 (2019) 29027–29033.

[60] G. McMahon, B. Miller, M. Burke, Correlative Nano SIMS and electron microscopy methods for understanding deuterium distributions after fatigue testing of 304/304L stainless steel in deuterated water, Int. J. Hydrogen Energy 45 (38) (2020) 20042–20052.

[61] S. Lynch, Environmentally assisted cracking: overview of evidence for an adsorption-induced localised-slip process, Acta Metall. 36 (10) (1988) 2639–2661.

[62] Y. Murakami, S. Matsuoka, Effect of hydrogen on fatigue crack growth of metals, Eng. Fract. Mech. 77 (2010) 1926–1940.

[63] X. Chen, C. Zhou, J. Zheng, L. Zhang, Effects of a′ martensite and deformation twin on hydrogen-assisted fatigue crack growth in cold/warm-rolled type 304 stainless steel, Int. J. Hydrogen Energy 43 (2018) 3342–3352.

[64] V. Shivanyuk, J. Foct, V. Gavriljuk, On a role of hydrogen-induced ε-martensite in embrittlement of stable austenitic steel, Scr. Mater. 49 (6) (2003) 601–606.

[65] M. Kamaya, Influence of mean strain on fatigue life of stainless steel in pressurized water reactor water environment, J. Press. Vessel Technol. 143 (2021).